Chemical Engineering Journal 165 (2010) 310–323

Contents lists available at ScienceDirect

Chemical Engineering Journal

journal homepage: www.elsevier.com/locate/cej

Characterizing the liquid dynamics in cocurrent gas–liquid flows in porous media using twin-plane electrical capacitance tomography

M. Hamidipour, F. Larachi*

Department of Chemical Engineering, Laval University, Québec, QC, G1V 0A6, Canada

ARTICLE INFO

Article history:
Received 6 March 2010
Received in revised form 4 August 2010
Accepted 24 August 2010

Keywords:
Hydrodynamics
Packed bed
Liquid holdup
Drainage
Electrical capacitance tomography

ABSTRACT

The hydrodynamics of gas–liquid cocurrent down- and upflow packed beds was studied experimentally using twin-plane electrical capacitance tomography (ECT). The ability of ECT to measure liquid holdups was examined by performing different calibration procedures. Confrontation of liquid holdup measurements from single-/twin-plane ECT, RTD and bed drainage revealed that ECT calibration between pre-wetted and flooded bed captured accurately the free-draining liquid holdups. A new modality of imaging tracer transients, referred to as twin-plane ECT/RTD, was proposed whereby upstream injections and detection of permittivity-contrasting liquid tracer impulsions allowed access, via voxel-affixed RTD and cross-correlation analyses, to interstitial velocity, liquid holdup and volumetric flux maps as well as to their degrees of uniformity. Single-plane ECT was successful at monitoring the liquid drainage dynamics showing its dependence with respect to gas flow rates and particle sizes, as well as to identify regime transitions and to unveil the relationships of pulse frequency and pulse velocity with respect to particle diameter and fluid throughputs in upflow and downflow.

1. Introduction

Randomly packed beds of catalyst particles have imposed themselves as the plough-horse in a very large portfolio of industrial applications, and in particular, in cocurrent gas–liquid flow operations [1]. Depending on whether full wetting of catalyst is desirable or not, gas and liquid may be contacted either cocurrently downwards or upwards [2,3]. It has become truistic nowadays to state that non-invasive techniques have become the tools of choice in pursuance of the detailed flow structures within porous media unlike the more traditional interfering probes inserted within flows. The number of research groups bending over to study non-invasively the gas–liquid flow structures in packed-bed reactors has been tremendous and has led to leap-frog advances in understanding their makings over the past years. Examples include the X-ray tomography/radiography studies by Marchot et al. [4] and recently by Van der Merwe et al. [5], γ-ray tomography [6,7], magnetic resonance imaging [8–10], and electrical capacitance tomography [11–13].

Thanks particularly to its high temporal resolution (up to 5 kHZ frame captures), electrical capacitance tomography (ECT) is being used in packed-bed research by several research groups, including ours. Reinecke and Mewes [11] monitored via ECT the passage of pulses in trickle beds unveiling their three-dimensional structure. Hamidipour et al. [12] tested the feasibility of ECT monitoring of fines deposition in trickle beds. Liu et al. [14] investigated the variations of liquid holdup along the trickle bed in slow mode liquid cyclic operation. They especially addressed the effect of split ratio and cycle time on flow maldistribution over the bed and reported that distribution imperfections were triggered during the draining period. Atta et al. [15] used ECT to examine the passage of solitary (both brief and long) liquid waves in base-peak cyclic operation of trickle beds. Their holdup trends were satisfactorily captured with Euler–Euler computational fluid dynamic (CFD) simulations. Matusiak et al. [16] recently compared liquid holdup measurements in trickle-bed reactors from capacitance wire mesh sensors and ECT. They concluded that both techniques measure satisfactorily liquid holdups, though with systematic over-predictions from ECT.

Although several studies have been performed in packed beds using ECT imaging, lack of consistency seems to emerge regarding the choice of calibration procedures and their impact on the liquid holdup estimation [14]. The aim of this work was first to compare two calibration approaches to identify which liquid holdup and saturation components are accessible from ECT. A new modality of imaging tracer transients, referred to as twin-plane ECT/RTD, was also proposed in which upstream injections and detection of permittivity-contrasting liquid tracer impulsions were used to estimate voxel-affixed interstitial velocities, liquid holdups and volumetric fluxes, as well as the degrees of uniformity of each one

---

* Corresponding author. Tel.: +1 418 656 3566; fax: +1 418 656 5993.
E-mail address: Faical.Larachi@gch.ulaval.ca (F. Larachi).

1385-8947/$ – see front matter © 2010 Elsevier B.V. All rights reserved.
doi:10.1016/j.cej.2010.08.058

Nomenclature

AARE	average absolute relative error, $\lvert\Sigma(y_i - x_i)/y_i\rvert$
A	constant in Eq. (12)
B	constant in Eq. (12)
C	constant in Eq. (12)
C_v	coefficient of variation (-)
$c(i,t)$	instantaneous tracer concentration within ith-voxel
e	electrical permittivity (F/m)
H	height
k	parameter in Eq. (15); liquid velocity, holdup or flux
M	molar mass (kg/mol)
N_V	number of voxels
NP	normalized permittivity (-)
$T_l(i)$	cross-correlation time between ECT signals from the corresponding ith-voxels (s)
U	superficial velocity (m/s)
u	pseudo-interstitial liquid velocity obtained from single-plane ECT measurements
v	pseudo-interstitial liquid velocity estimated from twin-plane ECT/RTD measurements
z	axial position (m)

Greek letters

β	liquid saturation (per unit bed void volume) (-)
δz_{probe}	RTD probe distance from bed edge (m)
ε	bed porosity (-)
ε_γ	γ-phase holdup (per unit reactor volume) (-)
μ	time-averaged liquid saturation (-)
ρ	density (kg/m^3)
σ	standard deviation of the instantaneous liquid saturation (-)
χ	degree of uniformity (-)

Superscripts

−[0]	dry bed
[0]	drained bed
[1]	flooded bed ($\varepsilon_g = 0$)
fd	free-draining
FoV	field of view
K	kerosene
o	voxel-scale value obtained from twin-plane ECT/RTD
res	residual (post-drainage)
st	static (from RTD)
T	tracer
u-l	upper plane-lower plane

Subscripts

bed	bed
g	gas
gl	gas–liquid
l	liquid
s	solid, superficial velocity

Acronyms

RTD	residence time distribution
ECT	electrical capacitance tomography

of them. The holdup and velocity results from single-plane ECT and twin-plane ECT/RTD measurements were then compared. Finally, using single-plane ECT measurements, the effect of particle size and gas superficial velocity on the dynamics of liquid drainage was studied experimentally along with the detection of flow regime changeover and pulse flow characteristics in cocurrent upflow and downflow operations.

Table 1
Physical properties of kerosene and RTD tracer.

Property	Kerosene	Tracer
Density (kg/m^3)	789	798
Viscosity (mPa s)	1.05	1.11
Surface tension (mN/m)	25.32	25.28

2. Experimental

Air–kerosene cocurrent downflow and upflow experiments were carried out at room temperature and atmospheric pressure using a 5.7 cm (ID) diameter Plexiglas column packed with 1, 2, 3 or 5 mm glass spheres (bed height, H_{bed} = 80 cm). The bed was immobilized by intertwining it between rigid lower and upper stainless steel grids. Liquid and gas in downflow were distributed, respectively, through a central spray nozzle and several small apertures evenly arranged through the cross-section [17]. In upflow, gas and liquid feeds passed through 10 cm of packing layer acting as a gas–liquid distributor and consisting of equally sized particles as the main bed ones.

A 2 × 12-electrode twin-plane electrical capacitance tomography (ECT) sensor (PTL300E with DAM200E sensor controller, Process Tomography Ltd.) was used for the determination of the liquid saturation distributions. The two rows of 5-cm high electrodes were bounded immediately above and below with 3.8-cm high guard electrodes to funnel the electric field nearby the active electrodes. The measured capacitances at given bed heights were used to reconstruct permittivity tomograms (32 × 32 voxels per image, $\delta x \times \delta y \times \delta z = 1.8\,\text{mm} \times 1.8\,\text{mm} \times 50\,\text{mm}$) out of which voxel phase volume fractions were inferred as described elsewhere [12,13]. The twin-plane configuration allowed capacitance measurements to be acquired by the 2 × 12 active electrodes at 50 tomographic scans per second simultaneously at two axial positions, z = 60 cm and z = 65 cm (from bed entrance).

In addition to liquid saturation estimations from single-plane ECT measurements, the twin-plane ECT setup can be taken advantage of in a dynamic mode by tracking transport between its two planes of *brief* tracer impulses injected upstream thus unveiling new forms of hydrodynamic properties to be described later. Two electrical conductivity probes inserted in the bed (δz_{probe} = 10 cm from each extremity of the bed) were also used to compare RTD-identified liquid holdups with the ECT-measured ones. For electrical conductivity and permittivity contrasts, a kerosene-based conductivity improver (SR 1795, Dorf Ketal Chemicals LLC, USA) was used as an electrolyte tracer and whose physical properties were adjusted, through dilution, to be similar to kerosene (Table 1).

For each row of the ECT electrodes, the averaging depth of the capacitance signals, referred to as the height of the field of view, H_{FoV}, was estimated through liquid free-draining tests using a packing-free liquid-full vertical column. The liquid-filled tube was allowed to drain at *constant* volumetric flow rates. Air-filled (empty) and kerosene-filled tube were assigned the lower- (e_g) and upper-limit (e_l) permittivity values, respectively. Hence once inside the H_{FoV} region, displacement of the gas–liquid interface position led to a two-phase compartment having a permittivity e_{gl}. Correspondingly, an evolving liquid volume fraction, ε_l, of the field of view was estimated as:

$$\varepsilon_l = \frac{e_{gl} - e_g}{e_l - e_g} \tag{1}$$

in which use was made of the assumption of a linearly barycentric mixture permittivity (e_{gl}) with permittivities of the constitutive phases weighted by their corresponding volume fractions.

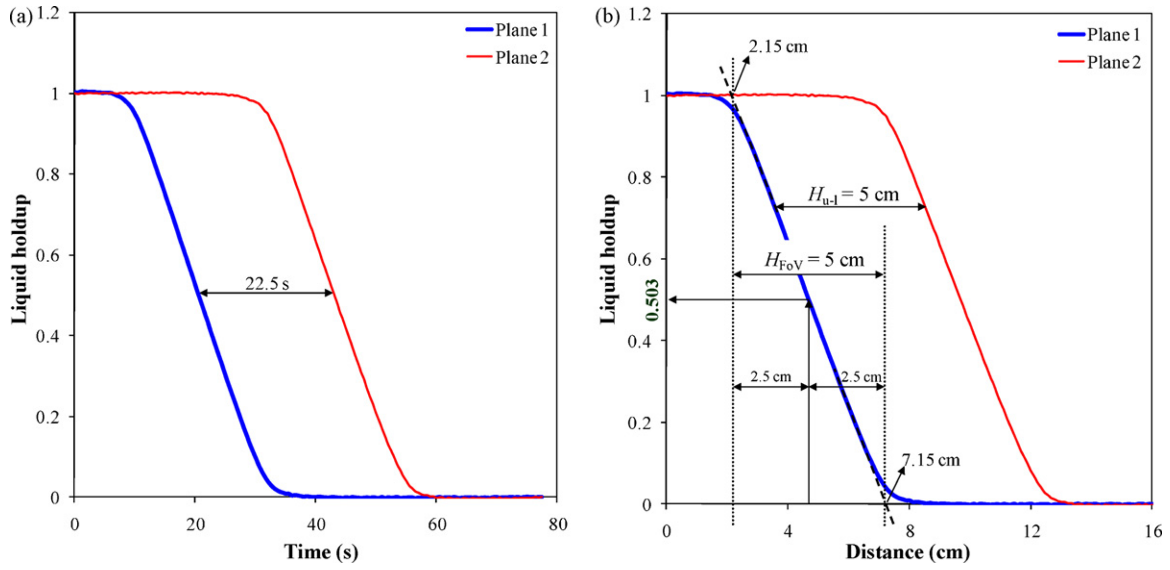

Fig. 1. Assessment of ECT sensor field of view height (H_{FoV}) via free-draining liquid holdup measurements in a vertical empty tube (a) time plot, (b) space plot.

The time of flight between ECT planes, estimated from Fig. 1a, was converted using the draining liquid volumetric flow rate into a space lag as shown in Fig. 1b. Edge effects contributed for ca. 0.9 cm for each side of the drainage curves (Fig. 1b). Excepting edge effects, H_{FoV} was estimated to be 5 cm (Fig. 1b) in agreement with the physical height of the electrodes provided by the manufacturer. Consistently, where the gas–liquid interface attained a mid-height, $H_{FoV}/2$, the liquid holdup Eq. (1) was equal to $0.50\underline{3}$ (Fig. 1b). Hence, this analysis revealed, on the one hand, that the linearly barycentric mixture permittivity relationship (Eq. (1)) was satisfactory for retrieving holdup from permittivities, and that the holdup measurements with our ECT will be, on the other hand, inescapably averaged over 5 cm high *voxels*. Since the (horizontal) pixel resolution was estimated to 3 mm [12], voxel discrimination cannot be better than 3 mm × 3 mm × 50 mm with our setup, which closely coincided with the voxel sizes of the discretized FoV. This undemanding drainage test also allowed to measure the separation distance between *u*pper and *l*ower rows of twin-plane ECT, $H_{u\text{-}l} = 5$ cm (Fig. 1b), as well as the interference distance common to the two rows of electrodes, ca. 0.85 cm or 17% × H_{FoV} (Fig. 1b). This distance for mutual interference was considered minor so that both FoVs were viewed as disjoint domains.

Liquid holdup measurements in the packed bed were thereafter carried out after the ECT sensor was calibrated at flooded (100%) and drained (0%) bed conditions. A plethora of mixing models is available in the literature to predict for the same multiphase or multicomponent mixture as many different effective permittivities. Though predictive methods for highly reliable predictions of mixture permittivity are not straightforward, fortunately mixture permittivities are loosely bounded between the so-called Wiener bounds [18]. In the above drainage test Eq. (1) (i.e., the Wiener upper-bound) was shown to be an *ad hoc* approximation although derivation of Eq. (1) rests on inclusion/matrix mixture capacitors mounted in a parallel circuit assuming aligned ellipsoidal inclusions and a depolarization factor 0 [18]. Extending the Wiener upper-bound effective permittivity to the packed-bed context, the *i*th-voxel barycentric mixture permittivities can be expressed as:

Flooded bed mixture permittivity

$$e^{[1]}(i) = (1-\varepsilon(i))e_s + \varepsilon(i)e_l \tag{2}$$

Drained-bed-mixture permittivity

$$e^{[0]}(i) = (1-\varepsilon(i))e_s + \varepsilon_l^{res}(i)e_l + (\varepsilon(i) - \varepsilon_l^{res}(i))e_g \tag{3}$$

Gas–liquid(–solid) flow mixture permittivity

$$e^{[gl]}(i) = (1-\varepsilon(i))e_s + (\varepsilon_l^{res}(i) + \varepsilon_l^{fd}(i))e_l + (\varepsilon(i) - \varepsilon_l^{res}(i) - \varepsilon_l^{fd}(i))e_g \tag{4}$$

where $\varepsilon(i)$, $\varepsilon_l^{res}(i)$, and $\varepsilon_l^{fd}(i)$, represent, respectively, the *i*th-voxel porosity, residual liquid holdup due to capillary forces and free-draining liquid holdup, and e_s, e_l, and e_g, the (non-porous) packing, liquid, and gas permittivities, respectively. Provided the mixture permittivities obey the above barycentric dependences, the *i*th-voxel normalized permittivity, $NP(i)$, (Eq. (5)) can be used to estimate the free-draining liquid holdup normalized by the effective bed porosity (after resting the residual liquid holdup), i.e., free-draining liquid saturation ($\beta^{fd}(i)$):

$$NP(i) = \frac{e^{[gl]}(i) - e^{[0]}(i)}{e^{[1]}(i) - e^{[0]}(i)} = \frac{\varepsilon_l^{fd}(i)}{\varepsilon(i) - \varepsilon_l^{res}(i)} = \beta^{fd}(i) \tag{5}$$

Obtainment of FoV-averaged free-draining liquid holdups, $\langle \varepsilon_l^{fd} \rangle$, using ECT free-draining liquid saturations (Eq. (5)) requires knowledge of the bed porosity, ε, and the residual liquid holdup, ε_l^{res}, both straightforwardly accessible otherwise:

$$\langle \varepsilon_l^{fd} \rangle = \frac{(\varepsilon - \varepsilon_l^{res})}{N_V} \sum_{i=1}^{N_V} \beta^{fd}(i) \tag{6}$$

where N_V denotes the number of voxels for a given row of electrodes.

3. Results and discussion

3.1. Confronting global liquid holdup measurements from single-plane ECT, RTD and bed drainage

The free-draining liquid holdups proceeding either from upper or lower single-plane ECT measurements unveiled similar values and are henceforth used indifferently. The recomposed total liquid holdups based on ECT-measured free-draining holdup (Eq. (6)), $\langle \varepsilon_l^{fd} \rangle$, and residual liquid holdup, ε_l^{res}, from bed drainage were confronted to the *total* liquid holdups measured from bed drainage ($\varepsilon_l^{fd}\big|_{drainage} + \varepsilon_l^{res}$), and to the RTD-inferred *total* liquid holdups, $\varepsilon_l|_{RTD}$. These latter were obtained from inlet and outlet electrical *conductivity* signals, measured using a pair of conductivity probes located at the bed extremities (imperfect tracer pulse method with downstream double-detection [19]), and that were interpreted by way of the plug flow with axial dispersion (PD) and the plug

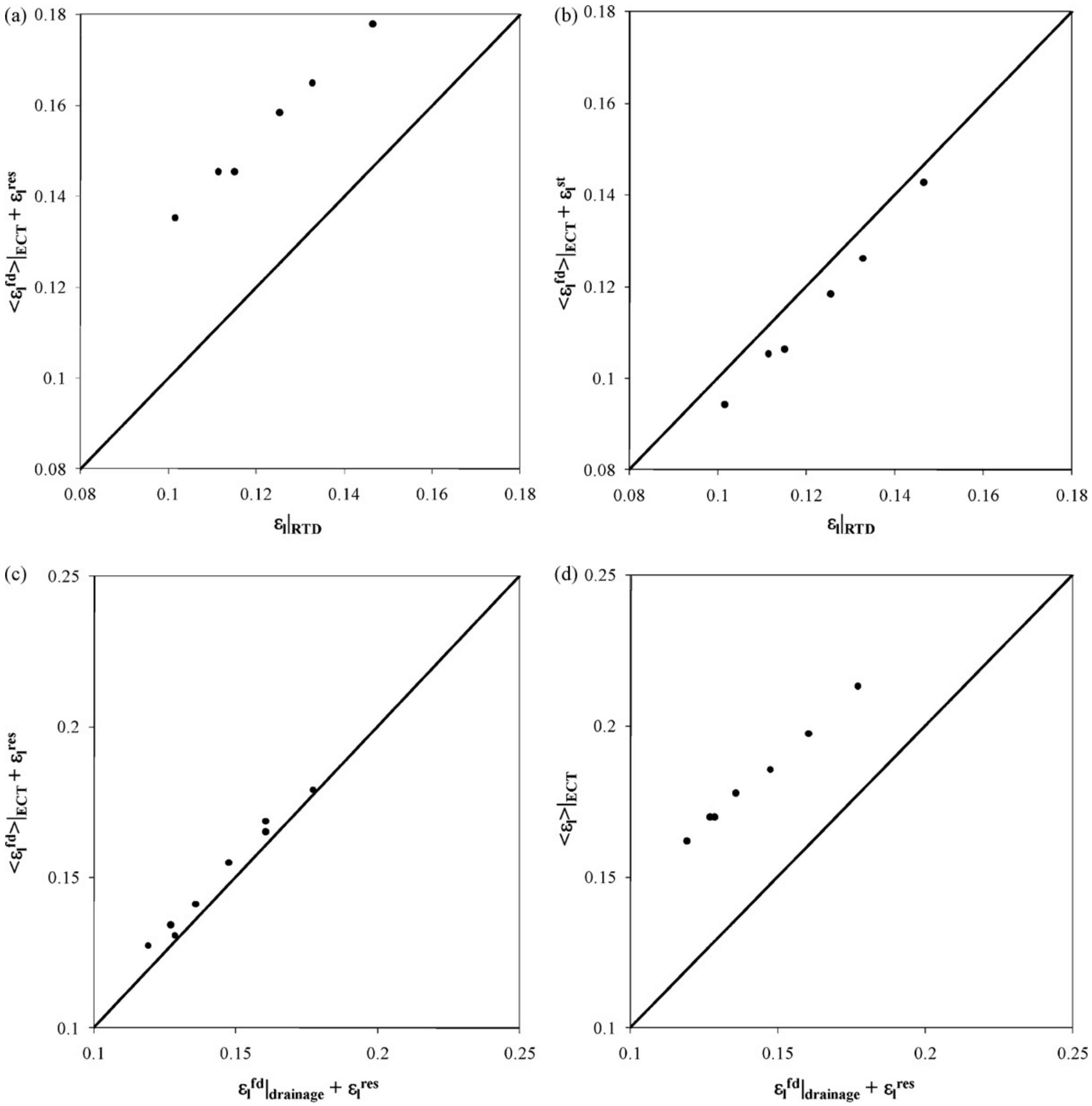

Fig. 2. Liquid holdup comparisons from ECT, RTD and drainage methods in trickle bed packed with 2 mm glass beads, (a) $\left\langle \varepsilon_l^{fd} \right\rangle\Big|_{ECT} + \varepsilon_l^{res}$ versus $\varepsilon_l|_{RTD}$, (b) $\left\langle \varepsilon_l^{fd} \right\rangle\Big|_{ECT} + \varepsilon_l^{st}$ versus $\varepsilon_l|_{RTD}$, (c) $\left\langle \varepsilon_l^{fd} \right\rangle\Big|_{ECT} + \varepsilon_l^{res}$ versus $\left\langle \varepsilon_l^{fd} \right\rangle\Big|_{drainage} + \varepsilon_l^{res}$, (d) $\langle \varepsilon_l \rangle|_{ECT}$ versus $\left\langle \varepsilon_l^{fd} \right\rangle\Big|_{drainage} + \varepsilon_l^{res}$.

flow with axial dispersion/mass exchange between dynamic and static zones (PDE) RTD models using open-open boundary conditions [20]. The PDE model, in addition to $\varepsilon_l|_{RTD}$, allowed estimation of the static liquid holdup, ε_l^{st}. The free-draining liquid holdups, $\varepsilon_l^{fd}\Big|_{drainage}$, were measured from bed drainage tests for the same sets of (U_g,U_l) and bed. The residual liquid holdup, ε_l^{res}, measured as the fraction of liquid volume (per unit reactor volume) that remained trapped in the bed after it was drained, was $\varepsilon_l^{res} \approx 0.048$. This value was in agreement with residual liquid holdup data for similar gas/liquid/solid systems reported in the literature [21]. At last, the global liquid holdup components averaged over FoV were distinguishable as $\left\langle \varepsilon_i^j \right\rangle$ from their bracket-free bed-averaged (RTD and bed drainage) homologues.

Fig. 2a shows that the recomposed total liquid holdups $\left\langle \varepsilon_l^{fd} \right\rangle\Big|_{ECT} + \varepsilon_l^{res}$ clearly exceeded their RTD-inferred counterparts, $\varepsilon_l|_{RTD}$. The average absolute relative error (AARE) between the holdups estimated by the two methods was substantial, AARE = 27.1%. The lack of agreement is possibly chargeable to RTD (impulse) techniques [22,23] whereby the brevity of tracer injections may sense only a fraction of the static liquid holdup, thereby underestimating the total (RTD) liquid holdup (Fig. 2a). Addition of static liquid holdup (ε_l^{st}), estimated via the PDE model, to $\left\langle \varepsilon_l^{fd} \right\rangle\Big|_{ECT}$ improved somehow the match with $\varepsilon_l|_{RTD}$ (AARE = 5.5%) as revealed from Fig. 2b parity plot. Nevertheless, in connection with the aforementioned underestimation, a slight negative bias between $\left\langle \varepsilon_l^{fd} \right\rangle\Big|_{ECT} + \varepsilon_l^{st}$ and $\varepsilon_l|_{RTD}$ was persistent. Thus, corroboration of global holdups from ECT (FoV-average, H_{FoV} = 5 cm) by means of tracer-impulse holdup estimations (bed-average, $H_{bed} - 2 \times \delta z_{probe}$) appears to be deficient to make sense of the ECT measurements.

Note for the moment that, being estimated differently and also because they refer to different averaging volumes, the free-draining liquid holdups measured from bed drainage, $\left\langle \varepsilon_l^{fd} \right\rangle\Big|_{drainage}$, may be different from the ECT-obtained $\left\langle \varepsilon_l^{fd} \right\rangle$. The best match of recom-

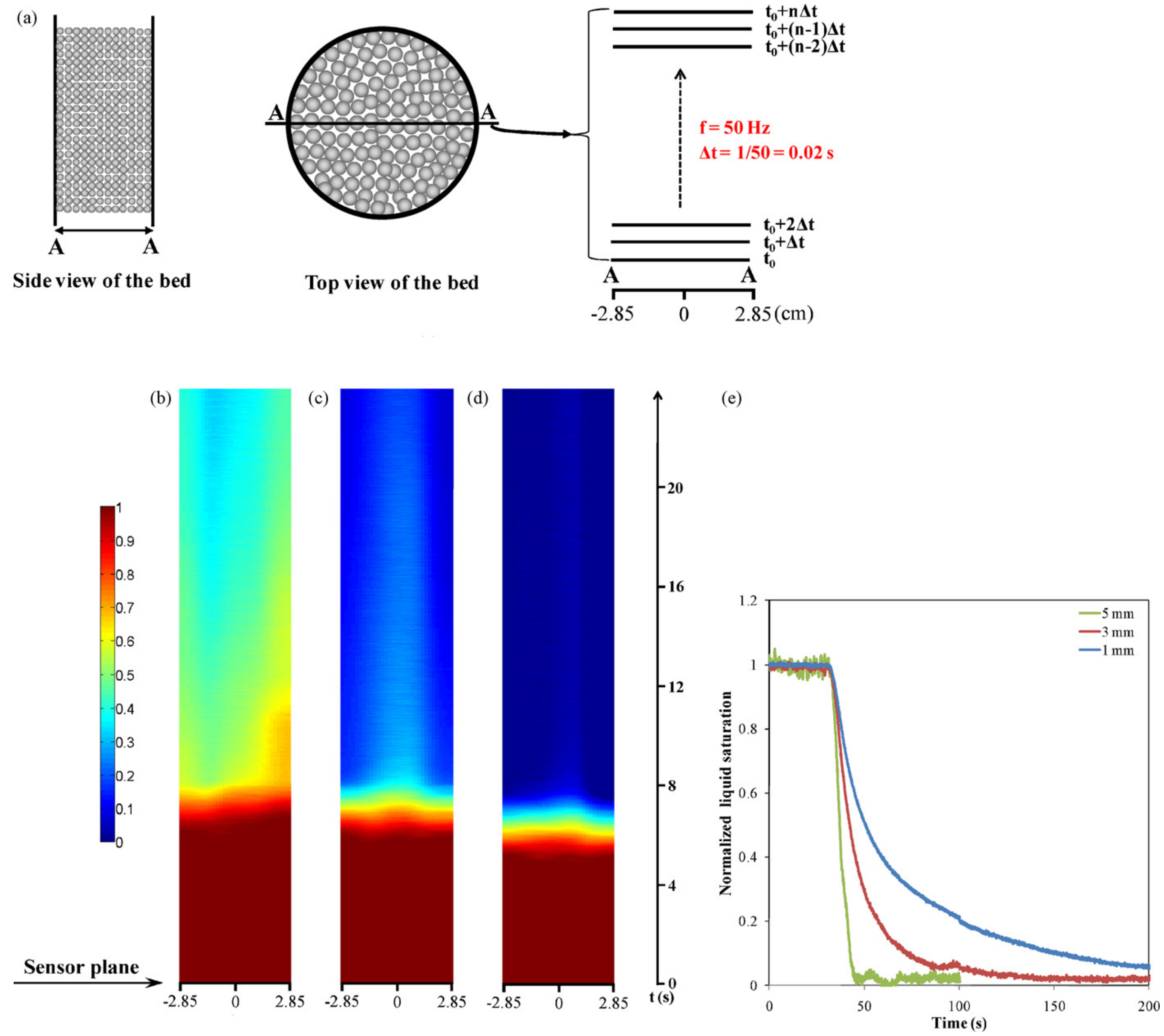

Fig. 3. (a) Construction of Eulerian slices, (b)–(d) instantaneous evolution of line A–A free-draining liquid saturation during drainage from flooded bed for 1 mm (b), 3 mm (c), and 5 mm (d), (e) for each particle size, instantaneous normalized (cross-section) liquid saturations were recorded for initially steady-state two-phase flow ($U_l = 0.0028$ m/s, $U_g = 0.062$ m/s) whereas during drainage only liquid feed was cut.

posed total liquid holdups was achieved between $\left\langle \varepsilon_l^{fd} \right\rangle\Big|_{ECT} + \varepsilon_l^{res}$ and $\left\langle \varepsilon_l^{fd} \right\rangle\Big|_{drainage} + \varepsilon_l^{res}$ as illustrated in Fig. 2c parity plot. The average absolute relative error between the holdups estimated by the two methods reduced in this case to 4.2%. Many factors would be in cause to explain the small deviations such as the approximate nature of the permittivity additivity law for the Wiener upper-bound [18], or the imperfections in image rendition (Tikhonov reconstruction algorithm, [13]) or even fluctuations of the bed properties (e.g., permeability, porosity, tortuosity, etc.) within FoV and whole bed domains. However, the positive bias was acceptably slim (Fig. 2c) to conclude that validation of the ECT-estimated integral holdups (Eq. (6)) is partially fulfilled with bed drainage measurements, i.e., $\left\langle \varepsilon_l^{fd} \right\rangle\Big|_{ECT} \approx \left\langle \varepsilon_l^{fd} \right\rangle\Big|_{drainage}$. By extension, the reconstructed voxel quantities given by Eq. (5) were also assumed to lead to free-draining saturations.

It could have been argued that replacing the drained-bed-mixture permittivity relationship Eq. (3) by a dry-bed-mixture permittivity:

$$e^{-[0]}(i) = (1-\varepsilon(i))e_s + \varepsilon(i)e_g \tag{7}$$

would have directly given access to total liquid saturations, $\beta(i)$, as ascertained from Eqs. (2), (4) and (7):

$$\frac{e^{[gl]}(i) - e^{-[0]}(i)}{e^{[1]}(i) - e^{-[0]}(i)} = \frac{\varepsilon_l^{fd}(i) + \varepsilon_l^{res}(i)}{\varepsilon(i)} = \frac{\varepsilon_l(i)}{\varepsilon(i)} = \beta(i) \tag{8}$$

Similarly to Eq. (6), the FoV-average total liquid holdup, $\langle\varepsilon_l\rangle$, using ECT local liquid saturations (Eq. (8)) could be cast as:

$$\langle\varepsilon_l\rangle = \frac{\varepsilon}{N_V}\sum_{i=1}^{N_V}\beta(i) \tag{9}$$

The normalization of permittivities using the set Eqs. (2), (4), (7) and (8) instead of Eqs. (2)–(5) for reconstructing liquid volume fractions were used by Liu et al. [14], and more recently by Matusiak et al. [16], who reported total liquid saturations (Eq. (8)) instead of free-draining liquid saturations (Eq. (5)).

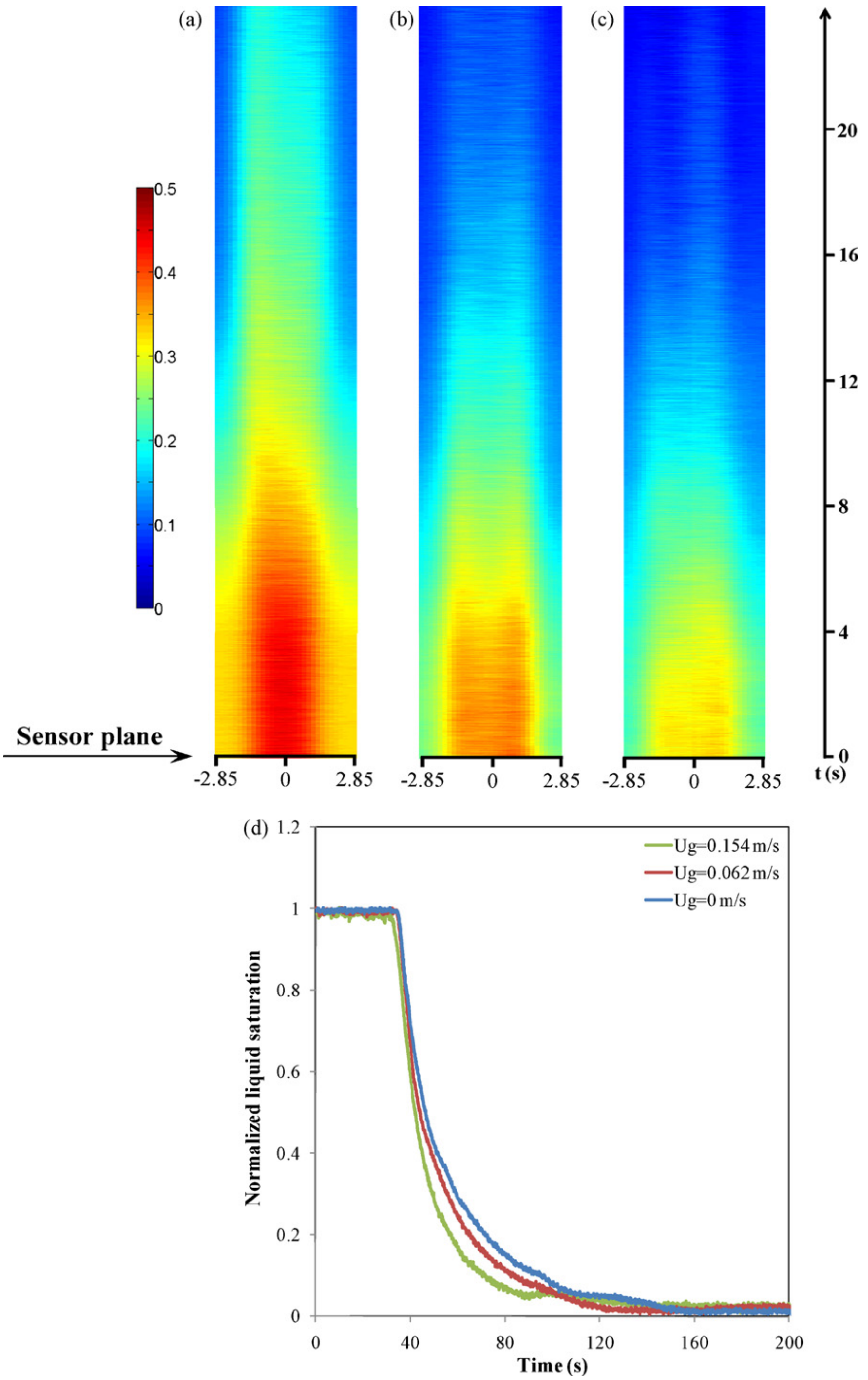

Fig. 4. (a)–(c) Instantaneous evolution of line A–A free-draining liquid saturation during drainage across 3 mm glass beads bed $U_g = 0$ (a), $U_g = 0.062$ (b), and $U_g = 0.154$ m/s (c), saturations recorded for initially steady-state two-phase flow ($U_l = 0.0028$ m/s, $U_g = 0, 0.062, 0.062$ m/s) whereas during drainage only liquid feed was cut, (d) instantaneous normalized (cross-section) liquid saturation during the same drainage tests.

Fig. 2d compares the total liquid holdups measured from bed drainage ($\varepsilon_l^{fd}\big|_{drainage} + \varepsilon_l^{res}$) to the total liquid holdup, $\langle\varepsilon_l\rangle|_{ECT}$, estimated from Eq. (9) and resulting from ECT calibration based on flooded (100%) and dry (0%) bed states (Eqs. (2) and (7)). The average absolute relative error between the holdups estimated by the two methods was 28.3% revealing that the ECT-based measurements exhibited, so far, the worst prediction performances along with an unacceptable positive bias (Fig. 2d). Inserting the drained bed in the ECT field of view led to an ECT-reconstructed residual liquid holdup amounting to $\left\langle\varepsilon_l^{res}\right\rangle\Big|_{ECT} \approx 0.091$. This was nearly twice the directly measured bed-averaged value, ε_l^{res}, reported earlier. Comparison between total liquid saturations from drainage, ($\varepsilon_l^{fd}\big|_{drainage} + \varepsilon_l^{res})/\varepsilon$, and those ECT-reconstructed saturations using Eqs. (2), (4), (7) and (8) was shown by Liu et al. [14] to suffer similar systematic positive biases, see their Fig. 5. Analogous over-prediction of ECT-reconstructed total liquid holdup (using the calibration set Eqs. (2), (4), (7) and (8)) with respect to the wire mesh measurement technique, chosen due to its higher spatial resolution, was also reported by Matusiak et al. [16]. No obvious reason was pinpointed for this inconsistency. It may be speculated that the interpolative

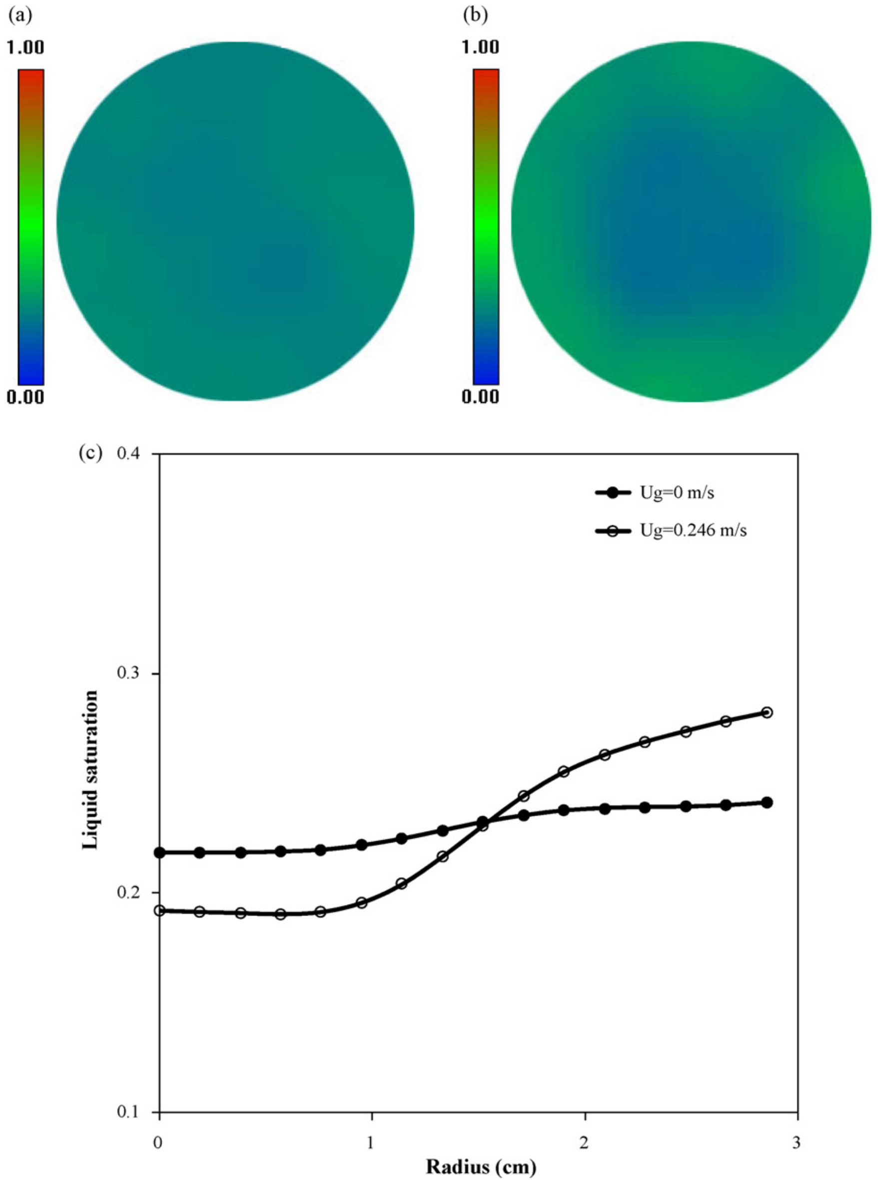

Fig. 5. (a) and (b) ECT normalized permittivity images and (c) corresponding radial distribution of residual liquid saturation, 1 mm glass beads, $U_g = 0$, 0.246 m/s.

character when the drained-bed-mixture permittivity (Eq. (3)) is used would lead to more reliably reconstructed liquid volume fractions instead of the dry-bed-mixture permittivity (Eq. (7)). In a sense, permittivity Eq. (4) interpolating between three-phase (Eq. (3)) and two-phase (Eq. (2)) systems proved to be more robust in lieu of interpolating between two-phase (Eqs. (2) and (7)) permittivity systems. Our study showed that calibrations based on drained pre-wetted bed and flooded bed proved to be more reliable and so experiments as reported here referred to single-plane ECT-estimated free-draining liquid holdups or saturations.

3.2. Liquid drainage dynamics

ECT was used to monitor the drainage dynamics at any desired height of the bed subsequently to liquid feed cut off and for sufficient time to assure that only the portion retained via capillarity was left. A useful representation of ECT images refers to Eulerian slices [11] where the voxel-based liquid saturations, reconstructed along a selected diametrical line (e.g., A–A line, Fig. 3a), are shot one after another at frame-capture frequency from the individual images. Evolving A–A line liquid saturations time-wise from bottom to top (Fig. 3a) would be equivalent to pick up delayed upstream events until they hit the tomograph field of view.

Fig. 3b–d shows Eulerian slices of free-draining liquid saturation taken at $z = 60$ cm for an initially flooded bed consisting of 1 mm, 3 mm and 5 mm glass beads, respectively. As particle size was increased, the drag force between liquid and solid diminished resulting in faster draining sequence. Lower liquid saturations nearby the wall area were clearly limned in the case of 3 mm and 5 mm glass beads in accordance with higher local porosities leading to eased liquid drainage. This was unlike the bed of 1 mm beads (column/particle diameter ratio = 57) for which the assumption of uniform porosity distribution looked more reasonable. Fig. 3e compares the cross-sectional average free-draining liquid saturation for 1 mm, 3 mm and 5 mm glass-bead packed beds when only liquid feed was interrupted while maintaining the gas flow uninterrupted through the bed ($U_g = 0.062$ m/s). Since different packing sizes resulted in different saturation dynamics, the saturation instantaneous values plotted in Fig. 3e were first normalized with respect to their minimum and maximum for each particle size. As in the case of gas-free drainage, starting from steady-state two-phase flow finer packings required longer times for the bed to drain.

Fig. 4a–c illustrates Eulerian slices of free-draining liquid saturation in a bed of 3 mm glass beads from the moment liquid flow was stopped under different gas superficial velocities (U_g = 0, 0.062, 0.154 m/s). The lower liquid saturations alongside the wall as a result of the larger porosity there were discernible. Also, increased gas velocities quickened the decrease of saturation as a result of applying higher shear force on the liquid phase. This resulted in steeper and briefer drainage sequences as confirmed in Fig. 4d. It is worthy of notice that the same residual liquid holdup value was reached no matter which gas velocity level was prevailing through the bed. This result agreed with findings by Lange et al. [24] who studied global liquid drainage behavior in trickle beds and reported that residual liquid holdup was unaffected by the gas superficial velocity level during liquid drainage step.

Although as explained earlier, ECT does not prove successful in capturing correctly the residual liquid saturation, the spatial distribution of local residual liquid saturations can at least be described qualitatively. Fig. 5a and b is contour plots of normalized permittivity images (or residual liquid holdups, obtained from Eq. (8)) subsequent to two drainage tests at U_g = 0 and 0.246 m/s. The corresponding azimuthally averaged radial distributions are presented in Fig. 5c. Under stagnant gas phase, the residual saturations denoted a relatively uniform distribution as a function of radial position in the bed. However, liquid drainage under gas flow induced a redistribution of residual liquid saturations. Hence, although the overall residual liquid saturations remained practically indifferent to U_g, it seems that gas flow affects the ultimate radial distribution of residual liquid saturations showing lower liquid retention in the bed core and higher closer to the wall.

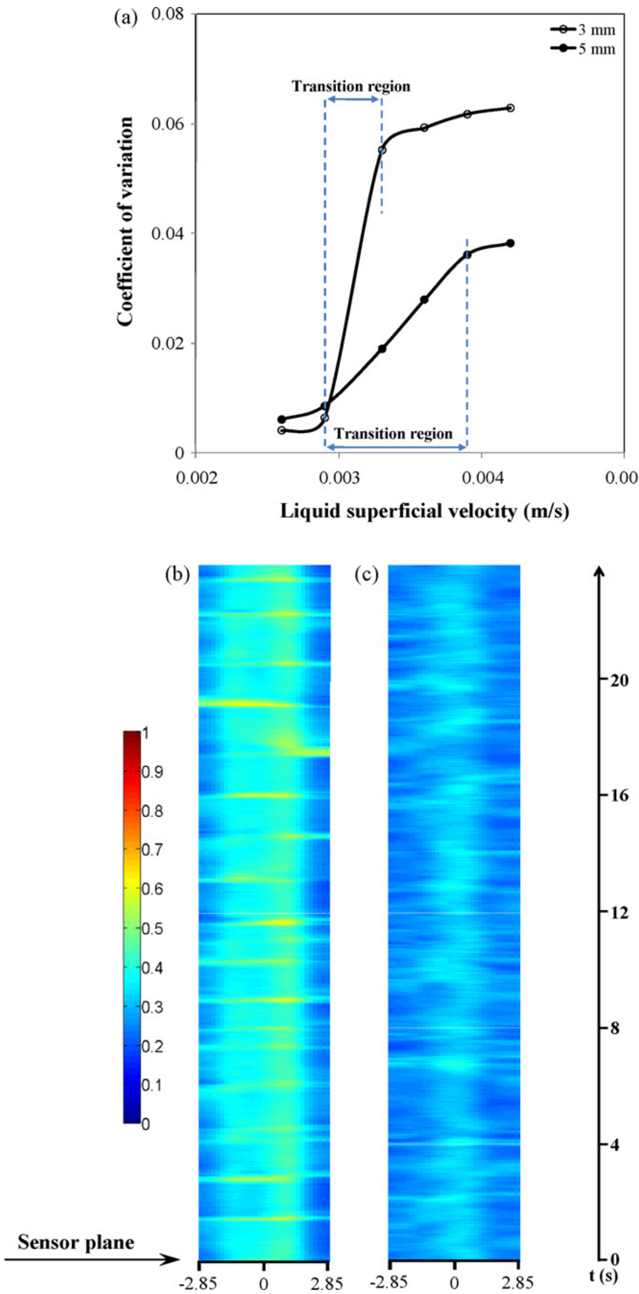

Fig. 6. (a) Criterion of trickle-to-pulse flow regime transition as a function of liquid superficial velocity and packing size, U_g = 0.062 m/s, (b) and (c) Eulerian slices of free-draining liquid saturation in pulse flow regime in cocurrent downflow, respectively, for 3 mm and 5 mm packing, U_l = 0.0042 m/s, U_g = 0.062 m/s.

3.3. Trickle-to-pulse and bubble-to-pulse flow regime transitions and pulse characteristics

Pulse flow regime is common to cocurrent gas–liquid downflow and upflow packed beds. Though the mechanisms subtending its inception in downflow and upflow are probably different, there are indications that packed-bed hydrodynamic characteristics (pressure drop, liquid holdup) in this high-interaction flow regime share some similarities [2]. The transitions between trickle flow and pulse flow in downflow and from dispersed bubble flow to pulse flow in upflow packed beds were delineated from the patterns arising in plots of a coefficient of variation, C_v, [25] of the ECT-reconstructed instantaneous liquid saturation signals. The coefficient of variation is simply defined as the ratio of the signal standard deviation, σ, over the time-average signal value, μ, $C_v = \sigma/\mu$.

Fig. 6a depicts the evolution of C_v as a function of liquid superficial velocity in cocurrent downflow for 3 mm and 5 mm glass beads (U_g = 0.062 m/s). A transition from trickle flow (low C_v) was detected at the same liquid velocity for both particle sizes. The ensuing transition area was sharper, narrower and more heightened for the smaller beads which implied stronger gas–liquid–solid interactions and allowed earlier attainment of the fully developed pulse flow regime. Eulerian slices of free-draining liquid saturation in pulse flow regime for 3 mm and 5 mm packing, respectively, are illustrated in Fig. 6b and c for U_l = 0.0042 m/s and U_g = 0.062 m/s. Differences between the horizontal streaks in Fig. 6b and c suggest that the pulse structure must be sensitive to particle size. However, the poor axial sensitivity of the measurement technique (H_{FoV} = 5 cm) did not allow to resolve precisely the liquid holdup content of the succeeding liquid rich slugs. The pulse velocity and frequency in pulse flow regime for the 3 mm and 5 mm packing size as a function of gas and liquid superficial velocities are shown in Fig. 7a and b. The air–kerosene system is known to be foaming which is especially awkward in the high-interaction regimes. However, no strong foaming was observed during the experiments as the operating conditions were set, according to Charpentier and Favier [26] flow map, close to the transition between pulsing and foaming-pulsing flow regimes. The pulse velocity was obtained knowing the separation distance, $H_{u\text{-}l}$, between the two sensor planes and obtaining the time delay for the pulses to cross it from cross-correlating the two per-plane liquid saturation time series. In agreement with literature findings [27,28], pulse velocity increases with decreasing particle size and increasing gas superficial velocity, though remaining indifferent to liquid superficial velocity (Fig. 7a). The aim of this work was to show the ability of ECT to measure the

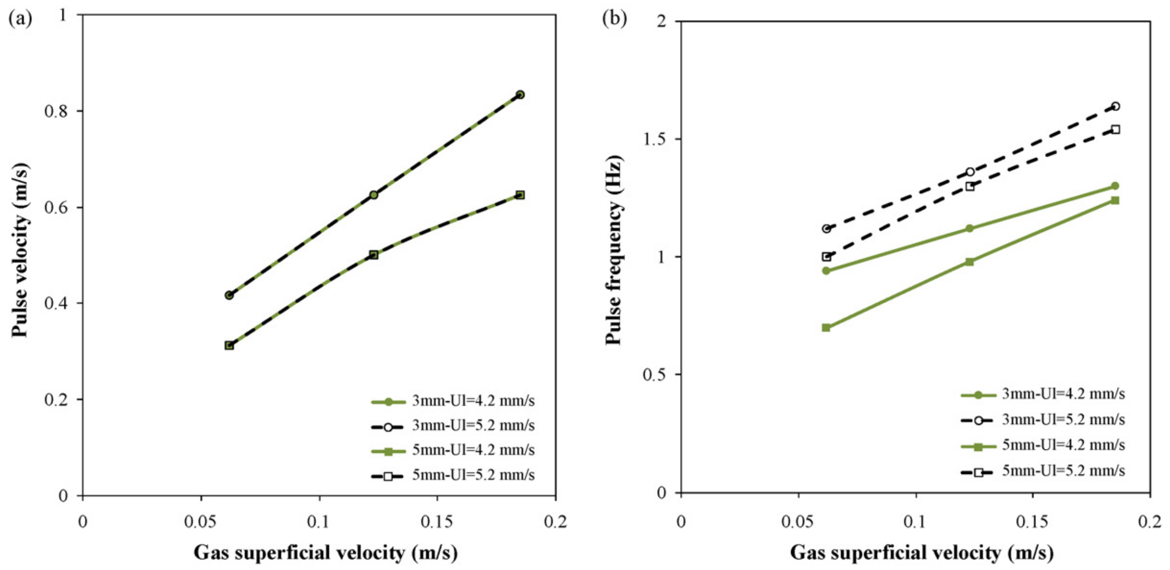

Fig. 7. (a) Pulse flow velocity and (b) pulse flow frequency in cocurrent downflow operation as a function of gas and liquid superficial velocities and packing size.

hydrodynamic parameters of the packed bed. Therefore, the range of selected operating conditions was *per se* not wide. The obtained information was in good agreement with existing literature data. Pulse frequency was obtained as the dominant frequency in the Fourier domain from the spectral power density of liquid saturation time series [12]. In line with the findings of Prof. Drinkenburg and Prof. Wild groups, using different measurement techniques, pulse frequency (Fig. 7b) increases as particle size decreases or as gas and liquid superficial velocities increase [27–29].

Dispersed bubble-to-pulse flow regime transition in cocurrent upflow operation is illustrated in Fig. 8a as a function of gas superficial velocity and a constant $U_l = 0.0029$ m/s. Similarly to downflow, the transition region to attain a developed pulse flow regime was wider for the larger packing size. It is worthy of notice that, for a given liquid superficial velocity, much lower gas superficial velocities are required to bring pulse regime in upflow than in downflow (Figs. 6a and 8a) much likely due to the higher liquid holdups prevailing in the former than in the latter. The structure of pulses depicted by the Eulerian slices of free-draining liquid saturations are shown in Fig. 8b and c for 3 mm and 5 mm glass beads, respectively. In spite of the poor axial sensitivity limitation, liquid slugs in cocurrent upflow can still be distinguished to carry larger liquid content than in downflow especially for the smaller packing sizes. Similarly with downflow operation, pulse velocity and frequency

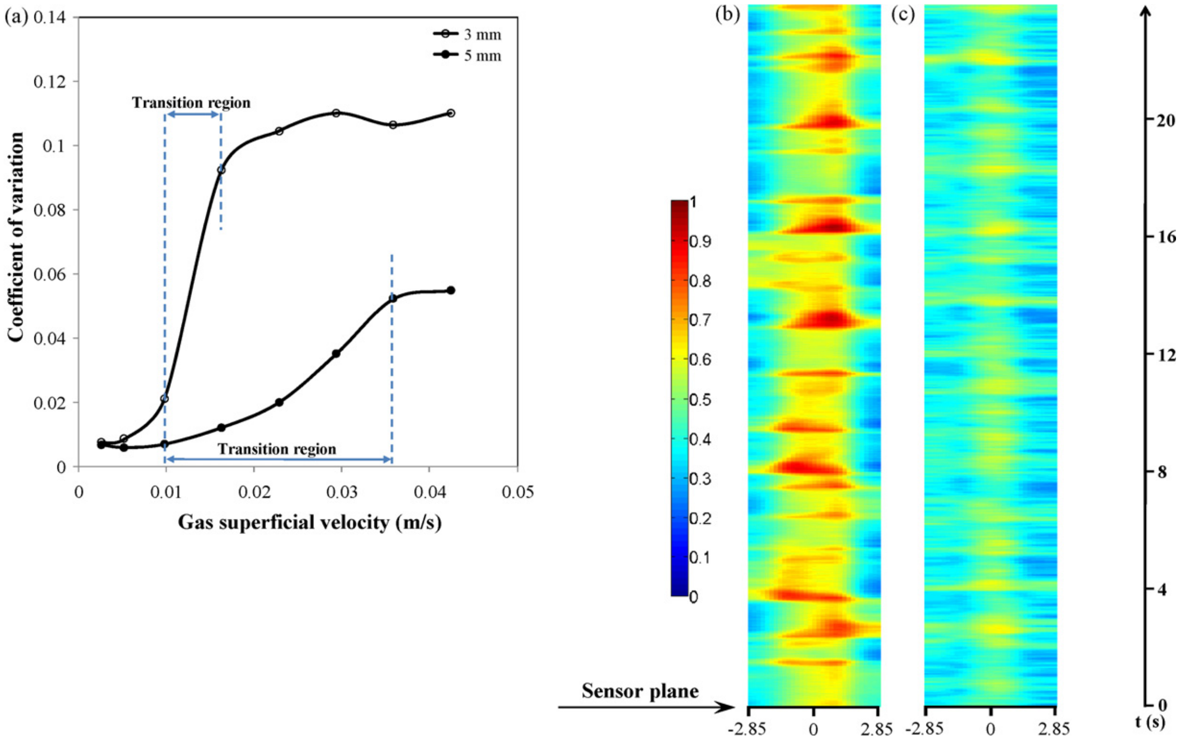

Fig. 8. (a) Criterion of dispersed bubble-to-pulse flow regime transition as a function of gas superficial velocity and packing size, $U_l = 0.0029$ m/s, (b) and (c) Eulerian slices of free-draining liquid saturation in pulse flow regime in cocurrent upflow, respectively, for 3 mm and 5 mm packing, $U_l = 0.0029$ m/s, $U_g = 0.042$ m/s.

increase with increased gas superficial velocity and with decreased particle size (Fig. 9).

3.4. *Liquid holdup and velocity measurements via ECT imaging of tracer injections*

The discrimination of phase volume fractions on the basis of permittivity (e.g., Eq. (4)) is classically exploited in electrical capacitance tomography imaging. One interesting overture to take advantage of twin-plane capacitance tomography consists of upstream injections and detection of permittivity-contrasting liquid tracer impulsions, yet with a supplementary benefit of extracting voxel-affixed RTD information, such as liquid holdup and interstitial velocity. The method can be viewed as an evolved imperfect pulse Aris method in which voxel inlet and outlet tracer response *permittivity* signals can be monitored. This modality of imaging tracer transients was referred to as twin-plane ECT/RTD and where the PD model was retained for data analysis.

The permittivity contrasts induced by instantaneous concentration changes, $c(i,t)$, at the voxel level of a liquid tracer pulse evolves Eq. (4) in the form:

$$e^{[\mathrm{gl}]}(i,t) = (1-\varepsilon(i))e_{\mathrm{s}} + \varepsilon_{\mathrm{l}}(i)e_{\mathrm{l}}(c(i,t)) + (\varepsilon(i)-\varepsilon_{\mathrm{l}}(i))e_{\mathrm{g}} \tag{10}$$

for which the tracer passage left the liquid properties seamless (Table 1), except for permittivity. Unlike in Eq. (4), to minimize the effects of hydrodynamic fluctuations via the holdup terms in Eq. (10), the tests were carried out in trickle (downflow) and in dispersed bubble (upflow) flow regimes.

Similarly, the FoV-averaged gas–liquid(–solid) mixture permittivity writes as:

$$\left\langle e^{[\mathrm{gl}]}(t)\right\rangle = \frac{1}{N_{\mathrm{V}}}\sum_{i=1}^{N_{\mathrm{v}}}\{\varepsilon_{\mathrm{l}}(i)e_{\mathrm{l}}(c(i,t))\} + \frac{1}{N_{\mathrm{V}}}\sum_{i=1}^{N_{\mathrm{v}}}\{(1-\varepsilon(i))e_{\mathrm{s}} + (\varepsilon(i)-\varepsilon_{\mathrm{l}}(i))e_{\mathrm{g}}\} \tag{11}$$

Usually, the homogeneous two-component liquid solution excess permittivity is modeled using Redlich–Kister correlations and where the mixture permittivity is the sum of an ideal mixture permittivity and an excess permittivity [30]. Assimilating the kerosene/tracer system to a binary mixture, one has:

$$e_{\mathrm{l}}(c(i,t)) = \underbrace{\left(1-\frac{M_{\mathrm{K}}}{\rho_{\mathrm{l}}}c(i,t)\right)e_{\mathrm{K}} + \frac{M_{\mathrm{K}}}{\rho_{\mathrm{l}}}c(i,t)e_{\mathrm{T}}}_{\text{ideal}} + \underbrace{\frac{M_{\mathrm{K}}}{\rho_{\mathrm{l}}}c(i,t)\left(1-\frac{M_{\mathrm{K}}}{\rho_{\mathrm{l}}}c(i,t)\right)\left(A+B\left(1-\frac{2M_{\mathrm{K}}}{\rho_{\mathrm{l}}}c(i,t)\right)+C\left(1-\frac{2M_{\mathrm{K}}}{\rho_{\mathrm{l}}}c(i,t)\right)^{2}\right)}_{\text{excess}} \tag{12}$$

in this equation, e_{T}, and e_{K}, designate, respectively, the tracer and kerosene permittivities, M_{K} and ρ_{l} stand for the liquid molar mass and density, and *A*, *B* and *C* are empirical constants.

Fig. 10a shows the time evolution of inlet (lower plane) and outlet (upper plane) FoV-averaged normalized (mixture) permittivities (as in Eq. (11)) in cocurrent upflow subsequent to pulse injection for a 1 mm glass-bead bed fed at $U_{\mathrm{l}} = 0.0028$ m/s and $U_{\mathrm{g}} = 0.0065$ m/s. The fitted liquid space time (τ_{l}) and Péclet number to predict the outlet permittivity, as shown in Fig. 10a, are physically sound (regardless of fit goodness) only if the proportionality between tracer concentration and measured mixture permittivity is fulfilled, that is only if the excess permittivity is null ($A = B = C = 0$, Eq. (12)).

The voxel-scale liquid holdup, $\varepsilon_{\mathrm{l}}^{\mathrm{o}}$, and the FoV-averaged liquid holdup, $\left\langle\varepsilon_{\mathrm{l}}^{\mathrm{o}}\right\rangle$, can be deduced from knowledge of the corresponding voxel-based, $\tau_{\mathrm{l}}(i)$, and global, τ_{l}, liquid space times fitted by means of the PD model:

$$\varepsilon_{\mathrm{l}}^{\mathrm{o}}(i) = \tau_{\mathrm{l}}(i)\frac{U_{\mathrm{l}}}{H_{\mathrm{u\text{-}l}}} \tag{13}$$

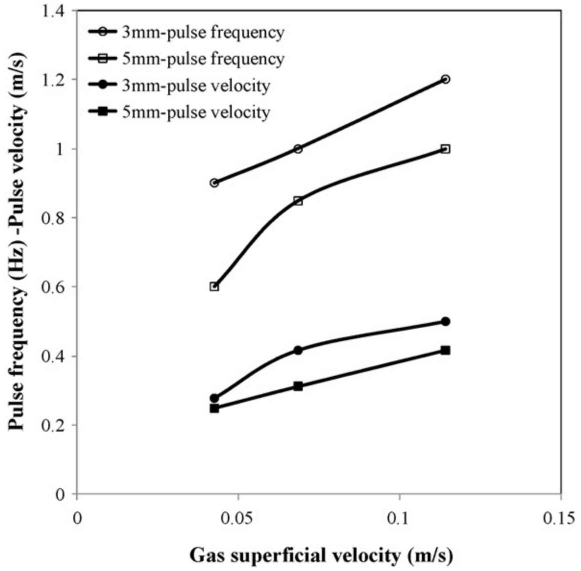

Fig. 9. Pulse flow velocity and frequency in concurrent upflow operation as a function of gas superficial velocity and packing size, $U_{\mathrm{l}} = 0.0029$ m/s.

$$\left\langle\varepsilon_{\mathrm{l}}^{\mathrm{o}}\right\rangle = \tau_{\mathrm{l}}\frac{U_{\mathrm{l}}}{H_{\mathrm{u\text{-}l}}} \tag{14}$$

Liquid holdups, $\left\langle\varepsilon_{\mathrm{l}}^{\mathrm{fd}}\right\rangle$, obtained from single-plane ECT according to the procedure explained in Section 3.1, were compared to liquid holdups, $\left\langle\varepsilon_{\mathrm{l}}^{\mathrm{o}}\right\rangle$, from twin-plane ECT/RTD (Eq. (14)) as displayed in Fig. 10b and c parity plots for cocurrent upflow and downflow. Whichever the prevailing flow direction, those plots indicate that the liquid holdups proceeding from the latter method coincided with the ones that emanated from the former one. Hence, $\left\langle\varepsilon_{\mathrm{l}}^{\mathrm{o}}\right\rangle$ was appreciably lower than the above-discussed RTD-inferred total liquid holdup, $\varepsilon_{\mathrm{l}}|_{\mathrm{RTD}}$. This finding could suggest that the truncated *linear* approximation of the mixture permittivity in Eq. (12) was untenable (in which case closeness between $\left\langle\varepsilon_{\mathrm{l}}^{\mathrm{o}}\right\rangle$ and $\left\langle\varepsilon_{\mathrm{l}}^{\mathrm{fd}}\right\rangle$ would have been fortuitous), or that the tracer could not reach the static liquid holdup domain to trigger permittivity changes there. Due to the short distance separating the two planes ($H_{\mathrm{u\text{-}l}} = 5$ cm), it might be reasonable that the tracer exchange between active and inactive holdups was insignificant turning the ECT/RTD blind to the static holdup.

Twin-plane ECT/RTD permittivity measurements were combined to accede the interstitial liquid velocity, $\langle u_{\mathrm{l}}{}^{\mathrm{o}}\rangle$. This latter was computed as $H_{\mathrm{l\text{-}u}}/T_{\mathrm{l}}$ in which T_{l} is the time for maximum cross-correlation between inlet and outlet permittivity signals such as those in Fig. 10a. Interstitial liquid velocity can alternatively be calculated as $\langle u_{\mathrm{l}}\rangle = U_{\mathrm{l}}/\left\langle\varepsilon_{\mathrm{l}}^{\mathrm{fd}}\right\rangle$ using the cross-sectionally averaged free-draining liquid saturation obtained from single-plane ECT experiments, see Section 3.1. The parity plots of Fig. 10b and c comparing liquid interstitial velocities calculated from dual-plane cross-correlation and single-plane free-draining saturation indicate these velocities were nearly equivalent $\left(\left\langle u_{\mathrm{l}}^{\mathrm{o}}\right\rangle \approx \langle u_{\mathrm{l}}\rangle\right)$ both in cocurrent upflow and downflow.

Using Eq. (5), voxel-reconstructed free-draining liquid saturations, β^{fd}, were converted into voxel-associated free-draining

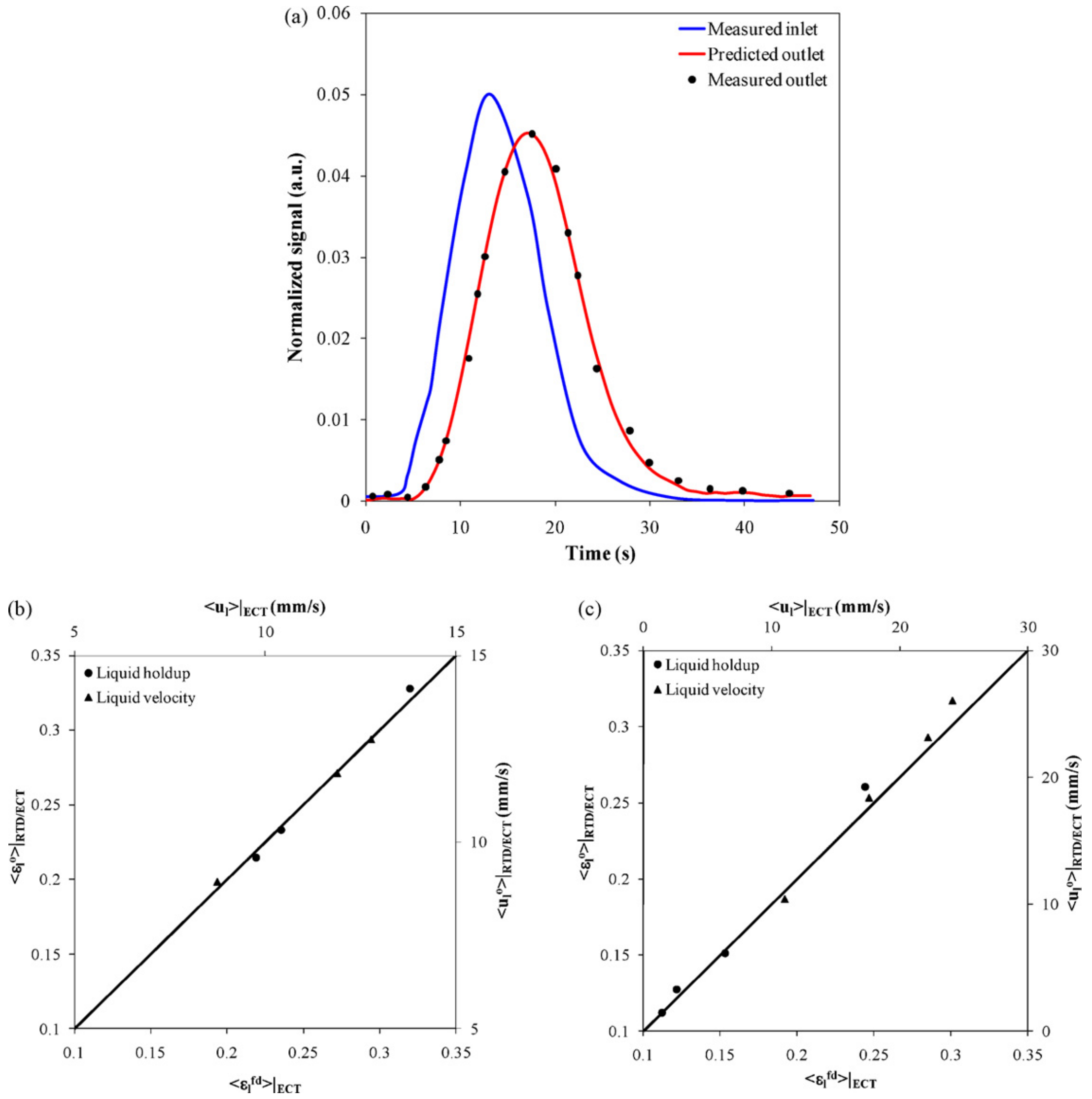

Fig. 10. (a) Experimental inlet and outlet ECT response curves subsequent to tracer injection together with the fit of outlet response using PD model, $U_l = 0.0028$ m/s, $U_g = 0.0065$ m/s, cocurrent upflow (b) parity plot of liquid holdup and interstitial velocity from single-plane saturation and dual-plane ECT RTD measurements ($U_l = 0.0028$ m/s, $U_g = 0$, 0.0013, 0.0065 m/s, cocurrent upflow, 1 mm glass beads), (c) parity plot liquid holdup and interstitial velocity from single-plane saturation and dual-plane cross-correlation measurements ($U_l = 0.0028$ m/s, $U_g = 0$, 0.062, 0.154, 0.246 m/s, cocurrent downflow, 1 mm glass beads).

liquid holdups, ε_l^{fd}, by substitution of bed residual liquid holdup and bed porosity. Hence pseudo-interstitial liquid velocities, u_i, were estimated from single-plane ECT as U_l/ε_l^{fd}, where two assumptions have been required: (i) transport of the whole liquid volumetric flux solely by the free-draining liquid, (ii) and voxel-invariant local volumetric flux of liquid, $U_l(i) = U_l$.

An alternate set of pseudo-interstitial liquid velocities, v_i, estimated from twin-plane ECT/RTD measurements was obtained as $H_{l\text{-}u}/T_l(i)$ where $T_l(i)$ is the time for maximum cross-correlation between inlet and outlet permittivity signals from the corresponding ith-voxels of upper and lower ECT planes.

Fig. 11(a1-4) and (b1-4) illustrates the contour plots of pseudo-interstitial liquid velocities u_i, and v_i, respectively, for various superficial gas velocities. The corresponding voxel-affixed free-draining liquid holdups obtained from single-plane ECT (ε_l^{fd}, Eq. (5)) and from twin-plane ECT/RTD (ε_l^{o}, Eq. (13)) are depicted in Fig. 12(a1-4) and (b1-4), respectively. For $U_g = 0$, both liquid pseudo-interstitial velocity and free-draining liquid holdup patterns were close to each other and their distributions showed the highest uniformity (Fig. 11a1 and b1, and Fig. 12a1 and b1). Increased gas flow rates had the tendency to lower the free-draining liquid holdup and to induce the largest liquid interstitial velocities nearby the wall regions. This trend was speculated to be ascribed to the fastest local gas flows due to some gas wall-flow short-circuiting in spite of a column/particle diameter ratio equal to 57. In general, the v_i plots deviated much farther from axisymmetric distributions than the u_i plots. Especially near the wall, the pseudo-interstitial velocities, v_i, were seen to exceed those estimated from single-plane ECT measurements. Also, liquid holdups with ECT/RTD modality were underestimated in the core and overestimated alongside the walls (Fig. 12(b2-4)) in comparison with their single-plane ECT homologues (Fig. 12(a2-4)). The (u_i,v_i) and (ε_l^{fd}, ε_l^{o}) distributions exhibited average liquid pseudo-interstitial velocity, respectively, $\langle u_l \rangle$ and $\left\langle u_l^{o} \right\rangle$, and the average liquid holdups, $\left\langle \varepsilon_l^{fd} \right\rangle$ and $\left\langle \varepsilon_l^{o} \right\rangle$, as discussed earlier (Fig. 10b and c).

To assess the capability of the ECT/RTD modality in retrieving the liquid volumetric flux from the simultaneous local measurements of $v_i(i)$ and $\varepsilon_l^{o}(i)$, the local volumetric flux of liquid, $U_l(i) = v_i(i) \cdot \varepsilon_l^{o}(i)$, traversing each voxel of the interrogated

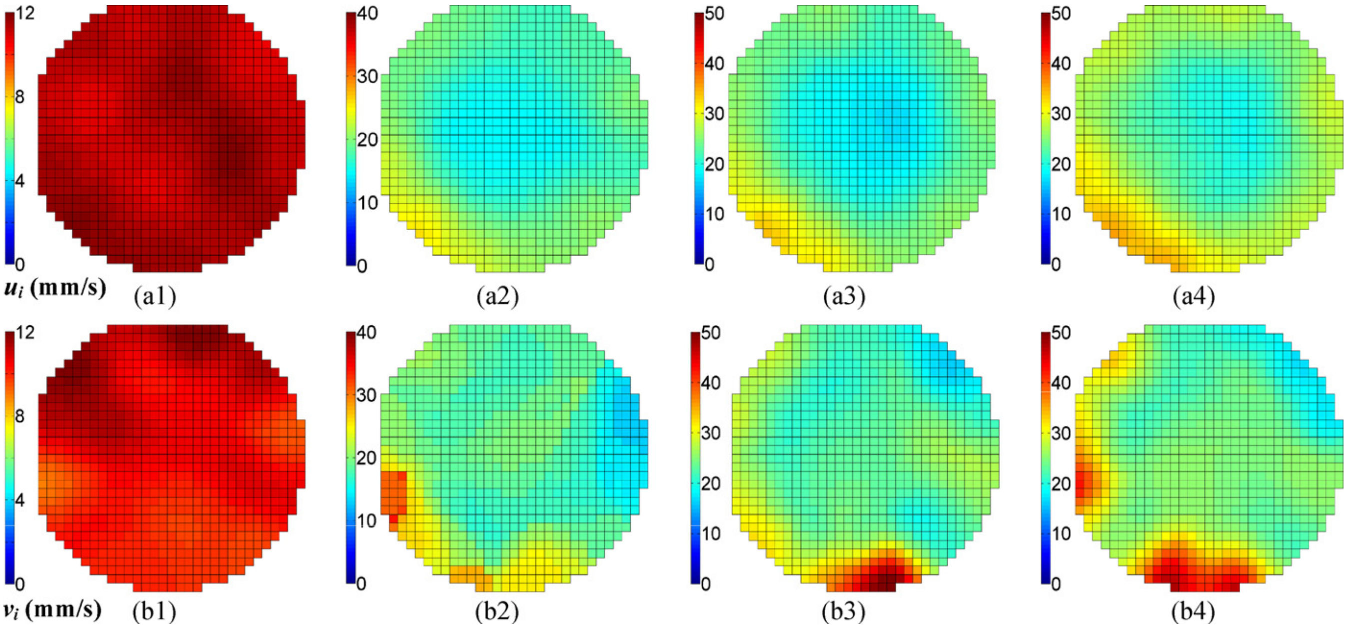

Fig. 11. Comparison of (a1-4) voxel-level interstitial liquid velocity from single-plane ECT, u_i, and (b1-4) from twin-plane ECT/RTD, v_i, 1 mm glass beads, $U_l = 0.0028$ m/s, $U_g = 0$, 0.062, 0.154, 0.246 m/s, cocurrent downflow.

domains was computed, respectively, for $U_g = 0$, 0.062, 0.154, 0.246 m/s and constant $U_l = 2.8$ mm/s in cocurrent downflow. The definitions of $v_i(i)$ and $\varepsilon_l^o(i)$ suggest that $U_l(i) = U_l \cdot \tau_l(i)/T_l(i)$. The corresponding $U_l(i)$ contour plots are shown in Fig. 13a–d for which the FoV averages, $\left\langle U_l \right\rangle = \left\langle v_i(i) \cdot \varepsilon_l^o(i) \right\rangle$, were found to be 2.789 ± 0.002 mm/s ($U_g = 0$ m/s), 2.929 ± 0.028 mm/s ($U_g = 0.062$ m/s), 2.958 ± 0.014 mm/s ($U_g = 0.154$ m/s) and 2.925 ± 0.011 mm/s ($U_g = 0.246$ m/s). Hence, in spite of the local disparities noted from the Fig. 13a–d contour plots, there is consistency between these averaged values, $\langle U_l \rangle$, and the actual liquid volumetric flux, U_l.

A statistical parameter, χ, as used by Patel et al. [31] was defined to express the extent of uniformity of calculated liquid interstitial velocity, holdup and flux from the twin-plane ECT/RTD measurements over the trickle-bed cross-section:

$$\chi = \frac{1}{N_v} \sum_{i=1}^{N_v} \left(\frac{k_i - \bar{k}}{\bar{k}} \right)^2 \qquad (15)$$

where k_i and $\bar{k}$ are, respectively, the local and the cross-sectionally averaged (velocity, holdup or flux) values. According to Eq. (15), χ approach to zero signifies improvement of distribution's uniformity for property, k. Confirming the above observations, Fig. 13e depicts the sensitivity of the degree of uniformity of $v_i(i)$, $\varepsilon_l^o(i)$ and $U_l(i)$ flux to the superficial gas velocity. In cocurrent downflow and at $U_g = 0$, $v_i(i)$, $\varepsilon_l^o(i)$ and $U_l(i)$ were highly uniform across the bed ECT-interrogated regions. Resuming gas flow induced deterioration in uniformity peaking near $U_g = 5$ cm/s for all three properties.

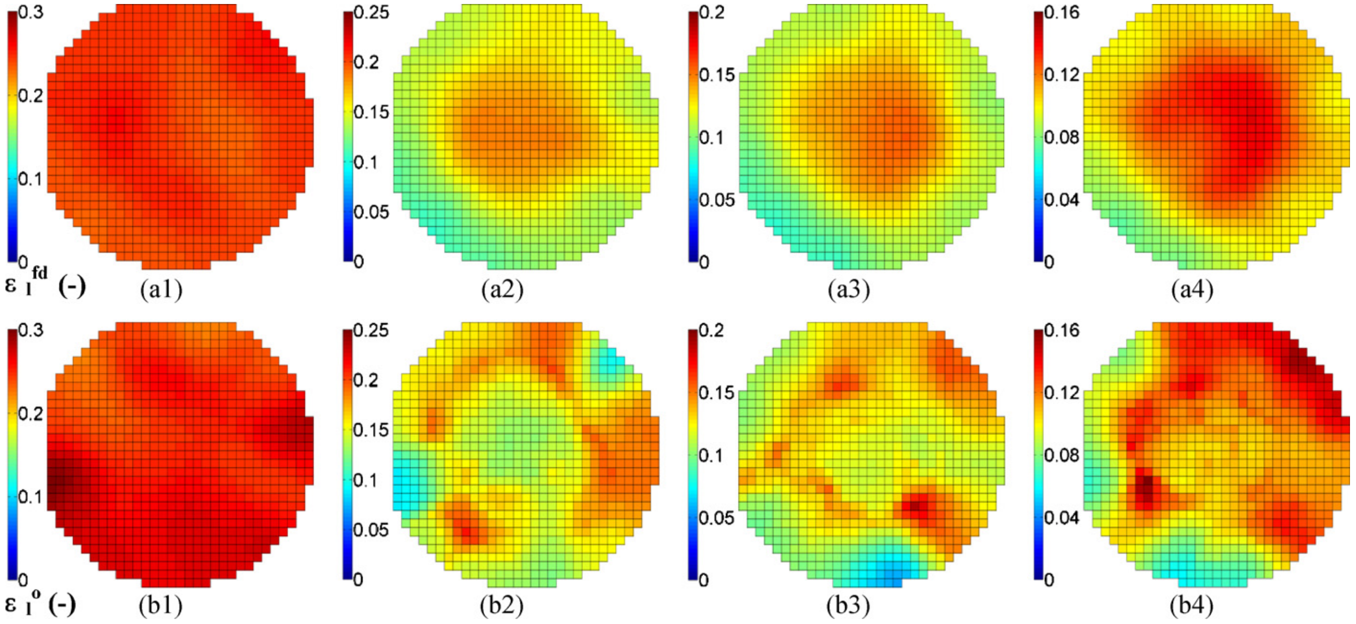

Fig. 12. Comparison of (a1-4) voxel-level free-draining liquid holdup, ε_l^{fd}, from single-plane ECT and (b1-4) twin-plane ECT/RTD, ε_l^o, 1 mm glass beads, $U_l = 0.0028$ m/s, $U_g = 0$, 0.062, 0.154, 0.246 m/s, cocurrent downflow.

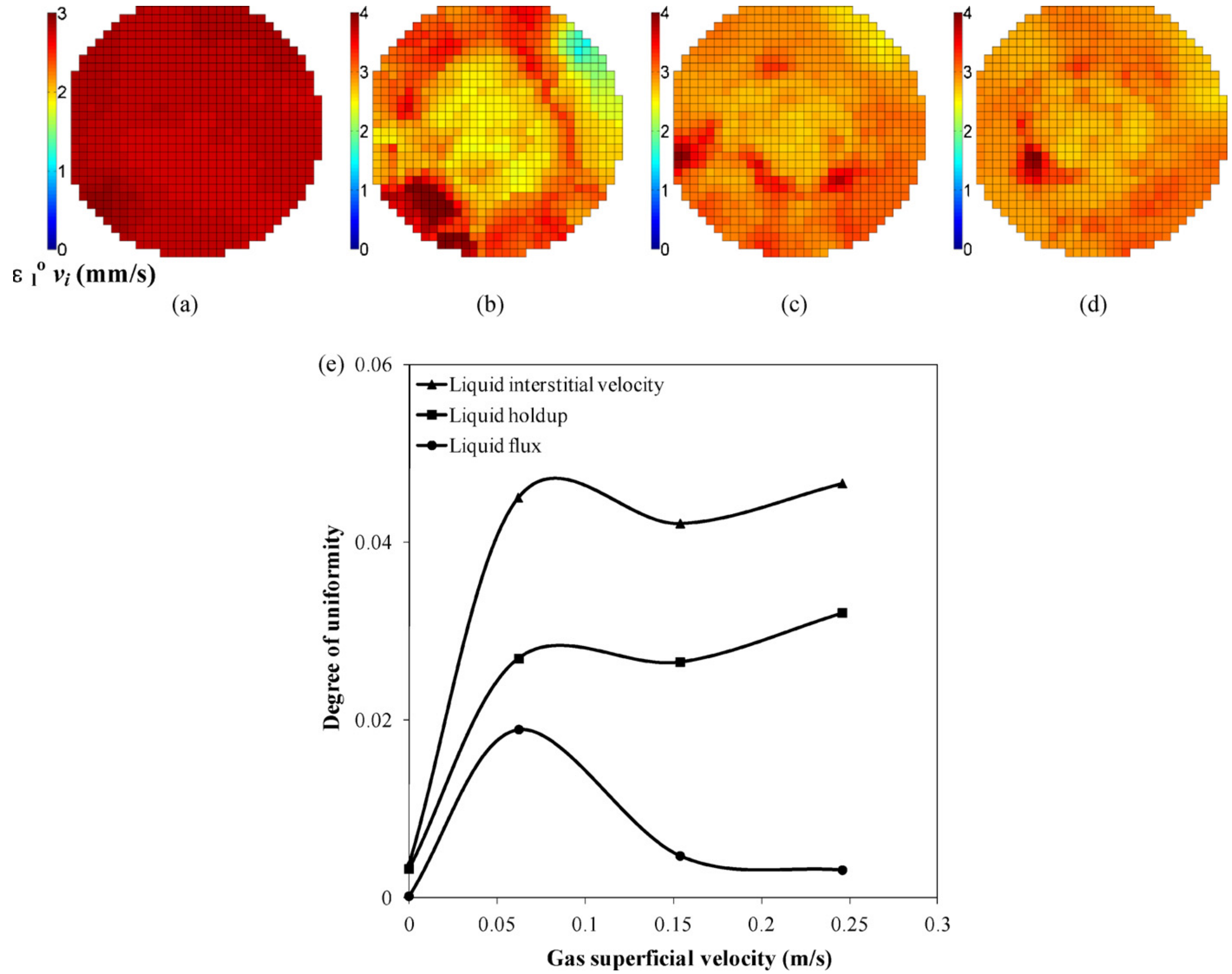

Fig. 13. (a)–(d) Voxel-based liquid fluxes computed as $U_l(i) = v_i(i) \cdot \varepsilon_l^o(i)$, 1 mm glass beads, $U_l = 0.0028$ m/s, $U_g = 0, 0.062, 0.154, 0.246$ m/s, (e) degree of uniformity $v_i(i)$, $\varepsilon_l^o(i)$, and $U_l(i)$ as a function of U_g, cocurrent downflow.

Further increases in gas superficial velocity lowered somewhat the criterion, χ, but it was the voxel-affixed interstitial velocity that showed the worst approach to homogeneity.

4. Conclusion

Dual-plane electrical capacitance tomography (ECT) was used to study the hydrodynamics of gas–liquid cocurrent packed-bed reactors. Different calibration approaches were examined to identify the parameters measurable via ECT imaging. Average and voxel-affixed liquid holdups and pseudo-interstitial velocities were obtained from single- and twin-plane ECT measurements using cross-correlation analysis and PD RTD model. The following conclusions were drawn:

- ECT calibration procedure performed using pre-wetted and flooded bed resulted in realistic free-draining liquid holdup measurements.
- A new modality of using twin-plane ECT, dubbed ECT/RTD, was proposed in which the dynamics of a soluble tracer in the liquid phase was imaged on the basis of permittivity contrasts detectable via ECT.
- Voxel-based RTD response curves enabled access to local liquid holdups from knowledge of the measured local liquid space times and liquid pseudo-interstitial velocities were obtained from cross-correlation between inlet and outlet voxel-based signals. Average liquid holdup and interstitial velocity obtained from twin-plane ECT/RTD were in fair agreement with single-plane ECT.
- The single-plane ECT revealed several new experimental information such as the dynamics of liquid drainage and its sensitivity to gas flow rates and particle sizes, the invariance of residual liquid holdup to prevailing gas superficial velocities, and the dependence of pulse frequency and velocity and flow regime transitions to fluid throughputs in downflow and upflow.

Acknowledgments

Financial support from the Canada Research Chair “Green processes for cleaner and sustainable energy” and the Discovery Grant from the Natural Sciences and Engineering Research Council (NSERC) is gratefully acknowledged. Dorf Ketal LLC (USA) is acknowledged for providing the conductivity improver (SR 1795). Prof. B. Riedl (Department of Wood Sciences) and Prof. D. Rodrigue

(Department of Chemical Engineering) are acknowledged for providing access to surface tension and viscosity measurements.

References

[1] M.P. Dudukovic, F. Larachi, P.L. Mills, Multiphase catalytic reactors: a perspective on current knowledge and future trends, Catal. Rev. Sci. Eng. 44 (2002) 123–246.

[2] X.L. Yang, G. Wild, J.P. Euzen, A comparison of the hydrodynamics of packed-bed reactors with cocurrent upflow and downflow of gas and liquid, Chem. Eng. Sci. 47 (1992) 1323–1325.

[3] M.R. Khadilkar, Y.X. Wu, M.H. Al-Dahhan, M.P. Dudukovic, M. Colakyan, Comparison of trickle-bed and upflow reactor performance at high pressure: model predictions and experimental observations, Chem. Eng. Sci. 51 (1996) 2139–2148.

[4] P. Marchot, D. Toye, A.M. Pelsser, M. Crine, G. L'Homme, Z. Olujic, Liquid distribution images on structured packing by X-ray computed tomography, AIChE J. 47 (2001) 1471–1476.

[5] W. Van der Merwe, W. Nicols, F. De Beer, Trickle flow distribution and stability by X-ray radiography, Chem. Eng. Sci. 132 (2007) 47–59.

[6] C. Boyer, A. Koudila, P. Chena, M.P. Dudukovic, Study of liquid spreading from a point source in a trickle bed via gamma-ray tomography and CFD simulation, Chem. Eng. Sci. 60 (2005) 6279–6288.

[7] M. Schubert, G. Hessel, C. Zippe, R. Lange, U. Hampel, Liquid flow texture analysis in trickle bed reactors using high-resolution gamma ray tomography, Chem. Eng. J. 140 (2008) 332–340.

[8] L.F. Gladden, H.H.M. Lim, M.D. Mantle, A.J. Sederman, E.H. Stitt, MRI visualization of two-phase flow in structured supports and trickle-bed reactors, Catal. Today 79–80 (2003) 203–210.

[9] I.V. Koptyug, A.A. Lysova, R.Z. Sagdeev, V.A. Kirillov, A.V. Kulikov, V.N. Parmon, In situ MRI of the structure and function of multiphase catalytic reactors, Catal. Today 105 (2005) 464–468.

[10] N.L. Nguyen, V. Van Buren, A. Von Garnier, E.H. Hardy, R. Reimert, Application of magnetic resonance imagining (MRI) for investigation of fluid dynamics in trickle bed reactors and of droplet separation kinetics in packed beds, Chem. Eng. Sci. 60 (2005) 6289–6297.

[11] N. Reinecke, D. Mewes, Investigation of the two-phase flow in trickle-bed reactors using capacitance tomography, Chem. Eng. Sci. 52 (1997) 2111–2127.

[12] M. Hamidipour, F. Larachi, Z. Ring, Monitoring filtration in trickle beds using electrical capacitance tomography, Ind. Eng. Chem. Res. 48 (2009) 1140–1153.

[13] C. Tibirna, D. Edouard, A. Fortin, F. Larachi, Usability of ECT for quantitative and qualitative characterization of trickle-bed flow dynamics subject to filtration conditions, Chem. Eng. Process. 45 (2006) 538–545.

[14] G. Liu, J. Lan, Y. Cao, Z. Huang, Z. Cheng, Z. Mi, New insights into transient behaviors of local liquid-holdup in periodically operated trickle-bed reactors using electrical capacitance tomography (ECT), Chem. Eng. Sci. 64 (2009) 3329–3343.

[15] A. Atta, M. Hamidipour, S. Roy, K.D.P. Nigam, F. Larachi, Propagation of slow/fast-mode solitary liquid waves in trickle beds via electrical capacitance tomography and computational fluid dynamics, Chem. Eng. Sci. 65 (2010) 1144–1150.

[16] B. Matusiak, M.J. da Silva, U. Hampel, A. Romanowski, Measurement of dynamic liquid distributions in a fixed bed using electrical capacitance tomography and capacitance wire-mesh sensor, Ind. Eng. Chem. Res. 49 (2010) 2070–2077.

[17] M. Hamidipour, F. Larachi, Z. Ring, Cyclic operation strategies in trickle beds & electrical capacitance tomography imaging of filtration dynamics, Ind. Eng. Chem. Res. 49 (2010) 934–952.

[18] K.K. Kärkkäinen, A.H. Sihvola, K.I. Nikoskinen, Effective permittivity of mixtures: numerical validation by the FDTD method, IEEE Trans. Geosci. Remote Sens. 38 (2000) 1303–1308.

[19] R. Aris, Notes on the diffusion-type model for longitudinal mixing in flow, Chem. Eng. Sci. 9 (1959) 266–267.

[20] J. Villermaux, W.P.M. Van Swaaij, Modèle représentatif de la distribution des temps de séjour dans un réacteur semi-infini à dispersion axiale avec zones stagnantes. Application à l'écoulement ruisselant dans des colonnes d'anneaux Raschig, Chem. Eng. Sci. 24 (1969) 1097–1111.

[21] J.C. Charpentier, M. Favier, Some liquid hold-up experimental data in trickle bed reactors for foaming and nonfoaming hydrocarbons, AIChE J. 21 (1975) 1213–1218.

[22] C.N. Schubert, J.R. Lindner, R.M. Kelly, Experimental methods for measuring static liquid holdup in packed columns, AIChE J. 32 (1986) 1920–1923.

[23] K.B. Kushalkar, V.G. Pangarkar, Liquid holdup and dispersion in packed columns, Chem. Eng. Sci. 45 (1990) 759–763.

[24] R. Lange, M. Schubert, T. Bauer, Liquid holdup in trickle-bed reactors at very low liquid Reynolds numbers, Ind. Eng. Chem. Res. 44 (2005) 6504–6508.

[25] B. Aydin, F. Larachi, Trickle bed hydrodynamics and flow regime transition at elevated temperature for a Newtonian and a non-Newtonian liquid, Chem. Eng. Sci. 60 (2005) 6687–6701.

[26] J.C. Charpentier, M. Favier, Some liquid holdup experimental data in trickle-bed reactors for foaming and non-foaming hydrocarbons, AIChE J. 21 (1975) 1213–1218.

[27] J.G. Boelhouwer, H.W. Piepers, A.A.H. Drinkenburg, Nature and characteristics of pulsing flow in trickle-bed reactors, Chem. Eng. Sci. 57 (2002) 4865–4876.

[28] J.R. Blok, A.A.H. Drinkenburg, Hydrodynamic properties of pulses in two-phase downflow operated packed columns, Chem. Eng. J. 25 (1982) 89–99.

[29] J.D. Llamas, F. Lesage, G. Wild, Local liquid saturation measurements inside a trickle bed reactor operating near the transition between pulsing and trickling flow, Chem. Eng. Sci. 62 (2007) 7225–7232.

[30] R.L. Smith Jr., S.B. Lee, H. Komori, K. Arai, Relative permittivity and dielectric relaxation in aqueous alcohol solutions, Fluid Phase Equilib. 144 (1998) 315–322.

[31] A.K. Patel, S.S. Waje, B.N. Thorat, A.S. Mujumdar, Tomographic diagnosis of gas maldistribution in gas–solid fluidized beds, Powder Technol. 185 (2008) 239–250.